Enhanced optical properties and (Zn, Mg) interdiffusion in vapour transport grown ZnO/MgO core/shell nanowires

2014 Nanotechnology 25 035705

(http://iopscience.iop.org/0957-4484/25/3/035705)

IOP Publishing Nanotechnology

Nanotechnology **25** (2014) 035705 (7pp) doi:10.1088/0957-4484/25/3/035705

Enhanced optical properties and (Zn, Mg) interdiffusion in vapour transport grown ZnO/MgO core/shell nanowires

G Grinblat[1,2], L J Borrero-González[3], L A O Nunes[3], M Tirado[4] and D Comedi[1,2]

[1] Laboratorio de Física del Sólido, Departamento de Física, FACET, Universidad Nacional de Tucumán, Avenida Independencia 1800, 4000 Tucumán, Argentina
[2] Consejo Nacional de Investigaciones Científicas y Técnicas (CONICET), Argentina
[3] Laboratório de Laser e Aplicações, Instituto de Física de São Carlos, Universidade de São Paulo, Avenida Trabalhador São-Carlense 400, CP 369, 13560-970 São Carlos, São Paulo, Brazil
[4] Laboratorio de Nanomateriales y de Propiedades Dieléctricas, Departamento de Física, FACET, Universidad Nacional de Tucumán, Avenida Independencia 1800, 4000 Tucumán, Argentina

E-mail: dcomedi@herrera.unt.edu.ar

Received 18 September 2013, revised 17 November 2013
Accepted for publication 2 December 2013
Published 20 December 2013

Abstract

ZnO/MgO (core/shell) nanowires (NWs) grown by a two-step vapour transport method under different MgO shell growth conditions are examined by x-ray diffraction, photoluminescence (PL) excitation and temperature (10–300 K) dependent PL. The excitonic-to-defect PL ratio is increased by more than two orders of magnitude in the core/shell as compared to bare ZnO NWs. Concomitantly, a strong depression of the PL thermal quenching, most particularly for the visible part of the PL spectrum, occurs. Using a semi-quantitative model, results are interpreted as a strong radiative to non-radiative lifetime ratio reduction due to defect passivation at the ZnO NW walls and photocarrier confinement within the ZnO core by the MgO shell. These beneficial effects are, however, significantly weakened when metal interdiffusion across the core/shell interface is favoured during the shell growth. Non-radiative recombination lifetime in the sample with sharp core/shell interface is described by a single activation energy of 15 meV (bound exciton release). For interdiffused cases and bare ZnO an additional activation energy of 60 meV (free exciton breakup) is observed.

Keywords: ZnO nanowires, core/shell nanowires, interdiffusion, photoluminescence

(Some figures may appear in colour only in the online journal)

1. Introduction

ZnO nanowires (NWs) have been intensively studied over the last decade due to their wide range of potential applications in optoelectronics, sensing, catalysis, and others [1]. Many years of research have shown that the effective passivation of NW walls to reduce density of surface states is crucial for applications in optoelectronics due to the large specific surface area of these nanostructures. Surface trap states shorten carrier lifetimes and are believed to be responsible for the well-known 'defect related' green luminescence [2, 3]. The MgO coating of the ZnO NW has been proved to reduce lasing thresholds and enhance excitonic photoluminescence (PL) [4, 5]. Since MgO bandgap is much larger than that of ZnO (∼7.8 eV as compared to ∼3.4 eV), the MgO shell provides confining barriers to electrons and holes within the ZnO core, thus favouring excitonic UV radiative recombination. Typically, hydrothermal [4] and electron beam evaporation synthesis [6] have been used to coat ZnO NWs with MgO. An attractive alternative are the vapour transport deposition (VTD) techniques, which are commonly used to grow high

quality ZnO and other NWs [5]. However, there is still a need to establish growth conditions that lead to effective carrier confinement and ZnO surface trap passivation leading to optimum excitonic emission. In particular, since VTD typically performs at several hundred degrees celsius, the possibility of interdiffusion across the ZnO/MgO interfaces during the shell growth needs to be considered.

In this paper, we apply a two-step VTD method for the growth of ZnO/MgO (core/shell) NWs, using different conditions for the MgO shell growth over the ZnO NWs. We discuss interdiffusion across the ZnO/MgO interfaces in terms of the MgO deposition parameters (temperature and time) and its influence on the PL and its temperature dependence. We present MgO deposition conditions that yield to a successful enhancement of the excitonic emission over the defect related luminescence. In these samples, a strong reduction of the PL thermal quenching is concomitantly observed, implying excellent passivation of surface defect states and photocarrier confinement. When the MgO deposition is carried out under conditions favouring interdiffusion between the oxides, these beneficial effects are partially inhibited. We quantify these effects using a recombination model which, in addition, enables us to determine non-radiative lifetime activation energies.

2. Experimental details

ZnO/MgO (core/shell) NWs were grown on Au-seeded Si substrates through two-step VTD. Si substrates were first covered with ∼5 nm Au-nanoclusters through DC magnetron sputtering deposition. Then, in a first growth stage, ZnO NWs were fabricated via Au-catalysed VTD [7] and, in a second step, MgO shells were grown over the ZnO NWs using the same deposition apparatus. The growth system comprises a continuously pumped quartz tube within a tubular furnace with mass flow controlled rates of Ar and O_2. An O_2/Ar flow rate ratio of 4% at a working pressure of ∼1 Torr was selected. For the first growth step, a crucible with the ZnO precursor powder (ZnO + C, 1:1 in weight) was placed at the furnace centre at 1000 °C, while the Au nanocluster seeded Si substrate was positioned 9 cm downstream the quartz tube, where the temperature was ∼900 °C due to a natural temperature gradient along the furnace axis. The Ar flux advects the Zn rich vapours from the crucible towards the substrate, while the O_2 gas compensates for the oxygen lost at the ZnO source by carbothermal reactions. After the ZnO NW growth, an annealing at 1000 °C was performed in the same Ar + O_2 atmosphere for several minutes. To study the MgO shell effects on the ZnO NWs, four different samples (S1, S2, S3 and S4) were fabricated. S_1 is a bare ZnO NW sample reference, while S_2, S_3 and S_4 are ZnO NW samples as S1 onto which MgO was deposited under different conditions (see table 1) in individual separate runs. Metallic Mg shavings were used as precursor, and the substrates were put at 1 cm downstream the Ar + O_2 flux direction, so the substrate temperatures were just slightly lower than that of the Mg source in all cases.

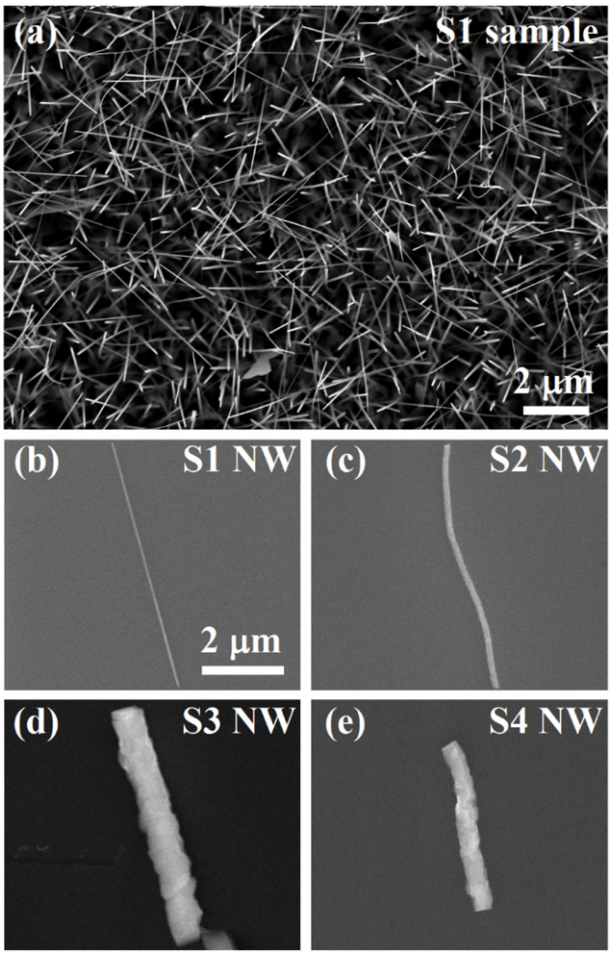

Figure 1. SEM images of the ZnO and ZnO/MgO NWs grown. (a) Top view of the reference sample S1. (b), (c), (d) and (e) show, respectively, isolated S1, S2, S3 and S4 NWs transferred from the original as-grown samples onto clean Si wafers. Scale bar in (b) refers to (c), (d) and (e) as well.

Table 1. MgO shell deposition parameters and final core/shell NW diameter (d) for all studied samples. T_{MgO} is the sample temperature during the MgO shell deposition and t_{MgO} is the total time each sample was held at T_{MgO} during and following the MgO shell deposition process.

Sample	T_{MgO} (°C)	t_{MgO} (min)	d (nm)
S1	—	—	∼50
S2	$\lesssim$1000	10	∼100
S3	$\lesssim\lesssim$700	10	∼700
S4	$\lesssim$1000	>60	∼400

NW morphologies were determined by scanning electron microscopy (SEM). Energy-dispersive x-ray spectroscopy confirmed the presence of Zn and O in S1, and of Zn, Mg and O in S2, S3 and S4. X-ray diffraction (XRD) measurements were performed using a Philips X'Pert Pro diffractometer. PL spectra in the 330–720 nm range were obtained using a He–Cd laser (Kimmon/IK5652R-G) at 325 nm as the excitation source. The luminescence signals were dispersed by a monochromator (0.3 m, Thermo Jarrell Ash/82497), detected with a photomultiplier tube (Hamamatsu/R928),

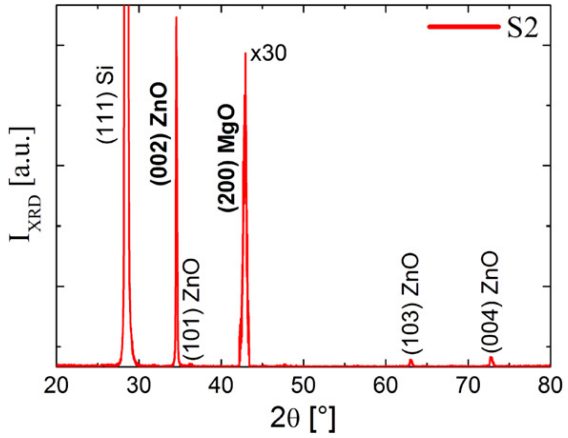

Figure 2. XRD data from sample S2. The (002) direction (hexagonal) is the most intense ZnO peak measured and the (200) direction (cubic) is the only MgO peak detected.

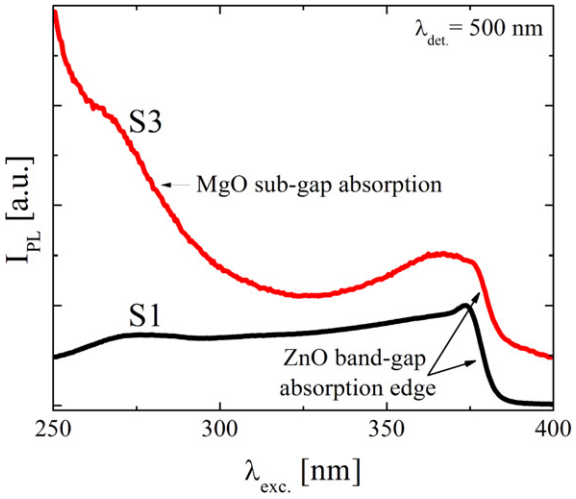

Figure 3. Room temperature PLE spectra from S1 and S3. ZnO band-edge absorption is observed for both samples, while MgO sub-gap absorption is only detected for S3.

and amplified using a lock-in amplifier. PL excitation (PLE) measurements were performed at $\lambda_{det} = 500$ nm within 250–400 nm excitation wavelength range using a SPEX FluoroLog spectrofluorometer (0.22 m, SPEX/1680) equipped with a Xe-lamp and a PMT/R928 detector.

3. Results

Table 1 shows the different conditions (temperature T_{MgO} and time t_{MgO}) prevailing during MgO deposition over the ZnO NWs for S2, S3 and S4, and the corresponding final mean NW diameters (d, as determined from SEM). The relatively short t_{MgO} for S2 and S3 stems from the fact that these samples were immediately quenched to room temperature after the shell deposition. S4, in turn, was kept for 60 min at ∼1000 °C and then let to cool down to room temperature slowly within the furnace under a static Ar + O_2 pressure of ∼1 Torr. As can be seen in table 1, S3 and S4 exhibit larger diameters than S2. This is due to a lower T_{MgO} for S3 (resulting in larger Mg supersaturation) and a longer t_{MgO} for S4.

Figure 1(a) shows a typical SEM plain view of as-grown NWs in S1. Figures 1(b), (c), (d) and (e) show, respectively, isolated NWs that were print transferred from S1, S2, S3 and S4 into clean Si substrates for a clear morphology appreciation. Due to ZnO and MgO lattice mismatch stresses, the composite ZnO/MgO NWs are slightly bent.

Both MgO and ZnO phases can be detected in the NW samples by XRD, as shown by the representative data in figure 2. The (002) reflection of hexagonal wurtzite is the most intense peak measured for ZnO, while the (200) reflection of the face-centred cubic structure is the only peak registered for MgO. This indicates strongly preferred growth directions, similar to reports in the literature for NWs also grown by a vapour transport method [5].

Typical PLE spectra are shown in figure 3 for S1 and S3. For comparison purposes, the spectra were normalized to have the same height at the ZnO bandgap absorption edge (∼380 nm), and then displaced vertically. As can be seen, the PL intensity increases with decreasing wavelength below ∼325 nm for S3. We attribute this effect to the onset of sub-gap absorption within the MgO shell in this sample (the MgO fundamental absorption edge at ∼159 nm cannot be detected in our experiment). Optical absorption measurements reported for MgO single crystals show similar results [8].

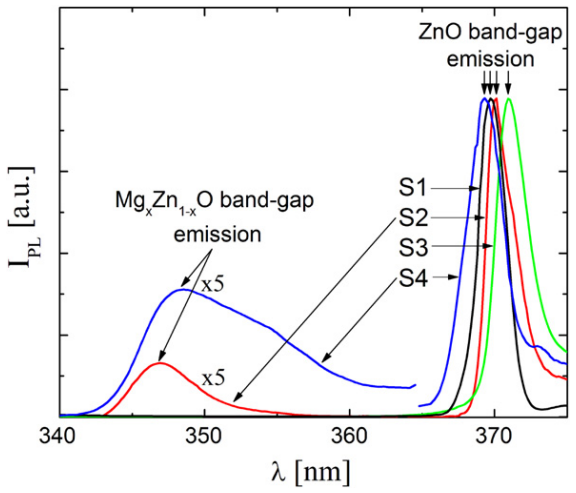

Figure 4. PL spectra in the UV range (normalized to have the same ZnO bandgap peak intensity) for all samples at $T = 10$ K. $Mg_xZn_{1-x}O$ bandgap luminescence is observed for S2 and S4, indicating interdiffusion between the ZnO core and MgO shell. No interdiffusion is detected for sample S3, consistent with the lower growth temperature of the MgO shell in this case.

Given the high temperatures involved in the MgO shell deposition, interdiffusion between the ZnO core and the MgO shell, producing $Mg_xZn_{1-x}O$ at the interface, may be expected. The presence of this ternary compound is not readily detectable through XRD, since the lattice symmetry and lattice parameter remain essentially unchanged between $x = 0$ and x up to ∼0.5 in $Mg_xZn_{1-x}O$ [9]. In this respect, PL studies are more useful because the bandgap of this compound is sensitive to the value of x [9–11].

Figure 4 shows PL spectra for all the samples in the UV region at $T = 10$ K. S2 and S4 ($T_{MgO} \approx 1000$ °C) exhibit

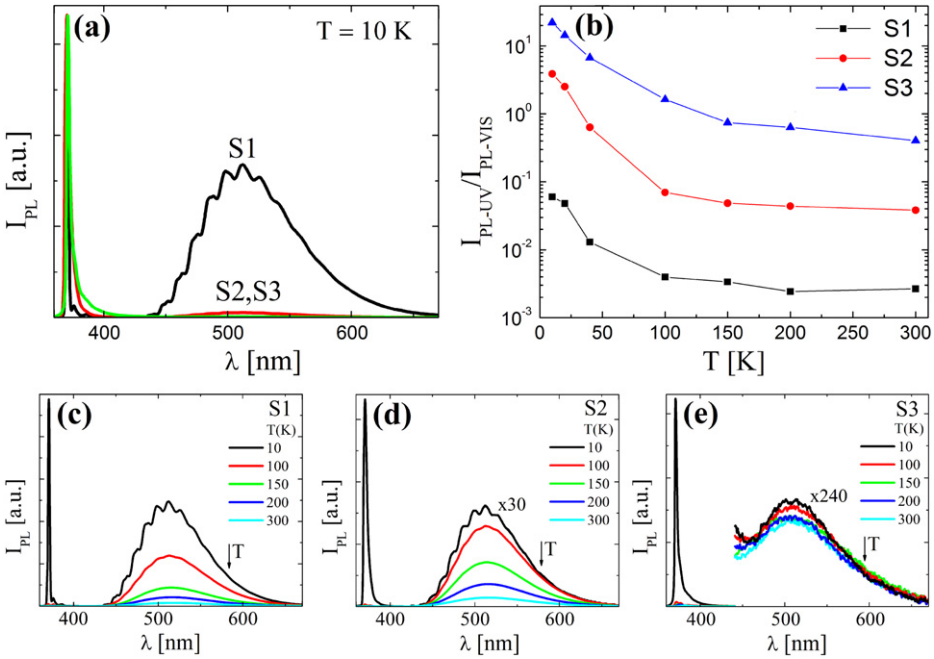

Figure 5. (a) PL spectra normalized by the ZnO bandgap peak intensity for samples S1, S2 and S3 at $T = 10$ K. (b) Temperature dependence of the integrated intensity of the UV band with respect to the visible (I_{PL-UV}/I_{PL-VIS}). (c), (d) and (e) show, for selected temperatures, the whole PL spectra for S1, S2 and S3, respectively. Direction of arrows indicates increasing temperature. Note that from sample S1 to S2, and then to S3, the PL band in the visible (∼520 nm) drops by more than two orders of magnitude.

luminescence related to $Mg_xZn_{1-x}O$ (the peaks between 340 and 360 nm), while S3 ($T_{MgO} \approx 700\,^{\circ}C$) does not. Indeed, Mg diffusion in ZnO has been reported to be very small at 700 °C [11, 12]. For S2, the ternary related peak centred at ∼347 nm indicates Mg incorporation in ZnO to about $x = 0.12$ [9]. This composition would imply a 2θ shift in the (200) ZnO XRD peak of only 0.1° [10], which is below the narrowest width observed in the XRD patterns. For S4, the corresponding spectrum in figure 4 shows a much broader $Mg_xZn_{1-x}O$ peak with an integrated intensity of ∼5 times that for S2. Due to a long effective t_{MgO} in this sample (see table 1), a large interdiffusion length may be expected [11], producing a wide ternary alloy interface that could include also distinct segregated phases [13]. For S2, in contrast, the ternary peak is much less intense and narrower, indicating a much narrower and probably more ordered interface. We see that, in summary, S2, S3 and S4 can be regarded as ZnO/MgO core/shell NW samples exhibiting some, negligible and strong interdiffusion, respectively.

The peaks at ∼370 nm in figure 4 are due to excitonic ZnO emission and their wavelength positions correspond closely to the bandgap energy. Those for both S2 and S3 exhibit small shifts to higher wavelengths as compared to S1. Similar shifts have been observed in bent [14] and stretched [15] ZnO NWs. We attribute the upward shifts to strains in the ZnO/MgO (core/shell) NWs, in consistency with the fact that these NWs are appreciably bent (see SEM images in figures 1(c) and (e)). Such strains could result from differences in thermal expansion coefficients or lattice size and symmetry mismatches between the ZnO core and the MgO shell. The smaller shift (∼0.3 nm) observed for S2 as compared to S3 (∼1 nm) is probably due to the intermediate interdiffused MgZnO layer at the ZnO/MgO interface in S2, not detected in S3, that reduces the interfacial stress on the ZnO core. As can also be seen in figure 4, the excitonic peak for S4 exhibits a small downward shift of the UV excitonic emission, which could be caused by some Mg incorporation into the ZnO core.

To characterize the MgO shell influence on the ZnO core emission properties, S1, S2 and S3 were selected for a careful study of the PL spectra at various temperatures. Figure 5(a) shows normalized PL spectra for these three samples at 10 K. It can be seen that the luminescence in the visible, typically associated with lattice defects, drops significantly when the ZnO NWs are covered with the MgO shell. As can be seen in figure 5(b), this reduction is by an order of magnitude for S2 (some interdiffusion) and more than two orders of magnitude for S3 (negligible interdiffusion) through the whole 10–300 K temperature range. This effect can be attributed to the passivation of deep defects at the ZnO NW surface by the MgO and the confinement of excited electrons and holes within the ZnO core by the MgO shell potential barrier. To be effective, the MgO shell needs to completely cover the ZnO core surface and be thick enough to form a tight potential barrier. Due to the high value of the potential barrier height expected for the ZnO/MgO core/shell system (≈2 eV), a very low escape (tunnelling) probability (of the order of 10^{-6}) can be calculated for a shell thickness as small as 1 nm. The MgO shell thicknesses in our samples are well above this value (see table 1). Since MgO is transparent to the ZnO emission (see figures 3 and 5(a)), there is not, in principle, an upper limit for this thickness. The weaker effect in S2 as compared to S3 can be expected, since interdiffusion in S2 leads to the blurring of the potential barrier at the ZnO/MgO

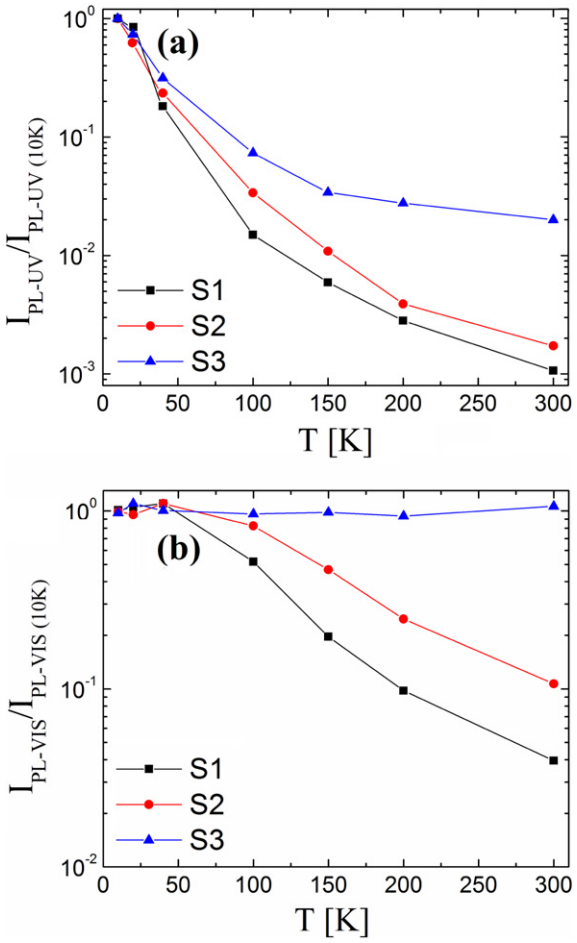

Figure 6. I_{PL-UV} (a) and I_{PL-VIS} (b) as a function of the sample temperature. Data sets are normalized by their corresponding values at 10 K. From sample S1 to S2, and then to S3, the thermal quenching is gradually depressed for both bands.

interface, reducing photocarrier confinement efficiency of the shell, thus enabling the penetration of electrons and holes into disordered ZnMgO interface regions and reducing the passivation effectiveness of the shell.

Figures 5(c), (d) and (e) show, respectively, the whole PL spectra for S1, S2 and S3 measured at selected temperatures in the 10–300 K range. In addition to reducing the defect related emission, the MgO shell also strongly reduces the temperature dependence of the PL intensity. For the case of S3 (negligible interdiffusion), the PL intensity of the defect band in the visible is even temperature independent. A similar behaviour is seen for the UV emission, although not as striking as for the emission in the visible. This can be more easily appreciated in figures 6(a) and (b), which show the temperature dependence of the integrated intensity of the UV (I_{PL-UV}) and defect (I_{PL-VIS}) bands. Again, S3 (negligible interdiffusion) exhibits a greater difference with respect to bare ZnO NWs than S2 (some interdiffusion). Reduced PL thermal quenching has been reported for ZnO/MgZnO (core/shell) NWs for the UV emission only [16, 17], and indicates increased (decreased) non-radiative (radiative) recombination lifetimes.

4. Discussion

The effects of the MgO shell on the ZnO core emission properties can be discussed in terms of a competition between non-radiative and radiative recombination processes. In general, non-radiative recombination may include Auger as well as non-radiative recombination processes through surface and/or defect states. Radiative recombination comprises mainly excitonic processes emitting in the UV and defect related ones usually emitting in the visible. Regarding the UV PL, recombination of excitons bound to impurity and defect centres dominates the spectrum at low temperatures [18]. As the temperature is raised, bound excitons are thermally activated into free excitons, which thermalize into states with $k \neq 0$ (wavevector, in particular its component along the NW axis) favouring non-radiative channels. Due to the large specific surface area in NWs, surface states are expected to play a major role as non-radiative recombination centres. Hence, the passivation of these surface states by the MgO shell and the resultant non-radiative lifetime increase are certainly behind the observed reduction of the PL thermal quenching in the ZnO/MgO (core/shell) NW samples. However, other hypothesis have also been proposed, such as exciton confinement, which is expected to enhance electron and hole wavefunction overlap within the ZnO NW core (decreasing the exciton radiative lifetime), and reduced exciton diffusion length due to the shell [16, 17].

In this respect, it is interesting to note that the temperature dependence of the visible PL band has received much less attention in the literature than that of the excitonic UV band. Nevertheless, its study could help elucidate the origin of the reduced thermal quenching of the PL. As seen in figure 6, the MgO shell effect on the defect band is stronger than on the UV emission; for S3 the quenching has been even removed completely (figure 6(b)). Since the visible luminescence originates preferentially at the NW surfaces [3], this indicates that passivation of non-radiative recombination surface states by the MgO shell is the main mechanism for the thermal quenching reduction. The other proposed mechanisms, such as carrier confinement and reduced diffusion length proposed previously for the UV PL, should not apply in this case since defect radiative recombination occurs through localized (surface) states.

It seems useful to use a simple model [19] to quantify changes that occur with the MgO shell deposition under different conditions. Given a certain transition involving an exciton density n and an exciton generation rate G, dynamic equilibrium requires:

$$\frac{\partial n}{\partial t} = G - \frac{n}{\tau_R} - \frac{n}{\tau_{NR}} \quad (1)$$

where τ_R and τ_{NR} are, respectively, radiative and non-radiative recombination lifetimes. Given that non-radiative recombination processes are usually thermally activated, τ_{NR} can be written as $\tau_{NR} = \tau_0 \exp(E_a/k_B T)$, where E_a is the activation energy for a determined non-radiative recombination channel and k_B is the Boltzmann constant. Since integrated PL intensities (I_{PL}) are proportional to n/τ_R,

then, at steady state (i.e. $\partial n/\partial t = 0$), considering a single non-radiative recombination channel, it follows that:

$$I_{\mathrm{PL}} = \frac{I_0}{1 + (\tau_{\mathrm{R}}/\tau_{\mathrm{NR}})} = \frac{I_0}{1 + r\exp(-E_{\mathrm{a}}/k_{\mathrm{b}}T)}, \quad \text{with } r = \tau_{\mathrm{R}}/\tau_0 \tag{2}$$

where I_0 is the integrated PL intensity at the low temperature limit.

Figure 7 shows the same data from figure 6(a), presented in a semilog plot as a function of the reciprocal temperature. The solid lines are fits using equation (2), and considering a temperature independent effective τ_{R}. Below 150 K, the $I_{\mathrm{PL-UV}}$ temperature dependence is well described by the model for all samples. The activation energy results to be $E_{\mathrm{a}} = 15$ meV for all the samples. This value coincides with those typically reported for bound exciton localization energies in ZnO [20], which is conceivable as bound exciton recombination dominates the UV PL at low temperatures. On the other hand, the model fits give values for r that differ from sample to sample (about 400, 200, and 100 for S1, S2, and S_3, respectively). Then, at low temperatures, r decreases by a factor of 2 (4) from sample S1 to S2 (S3). Above 150 K, equation (2) does not fit the PL thermal quenching for samples S1 and S2 (see encircled data at the figure). This indicates the presence of an additional non-radiative recombination channel with higher activation energy that starts to contribute significantly in this temperature range. To account for this effect, an extra exponential term must be added into the quotient of equation (2):

$$I_{\mathrm{PL}} = \frac{I_0}{1 + r\exp(-E_{\mathrm{a}}/k_{\mathrm{b}}T) + r'\exp(-E'_{\mathrm{a}}/k_{\mathrm{b}}T)}. \tag{3}$$

The inset of figure 7 shows the fits for samples S1 and S2 by using the modified equation (2). The activation energy of the extra term results to be $E'_{\mathrm{a}} = 60$ meV, which coincides with the exciton binding energy. With respect to r', it is found to be about an order of magnitude larger than r for both samples. This is reasonable, as uncorrelated electron–hole pairs are usually much more prone to recombine non-radiatively than excitons. Furthermore, the ratio $r'_{\mathrm{S2}}/r'_{\mathrm{S1}}$ turns out to be very close to $r_{\mathrm{S2}}/r_{\mathrm{S1}}$ (∼2).

Remarkably, S3 presents a very distinct behaviour. First, equation (2) describes correctly its UV-PL temperature dependence for the whole temperature range. Second, if one tries using equation (3) (with $E'_{\mathrm{a}} = 60$ meV) to fit the experimental data, the line remains identical to that as calculated with equation (2) (and hence the fit remains satisfactory below 300 K), as long as $r' \lesssim r$ is considered, but is appreciably worsened for $r' > r$. An alternative way to render the free exciton term negligible would be to consider an exciton binding energy larger than $E'_{\mathrm{a}} = 60$ meV, which could in principle result from exciton quantum confinement. However, this is not plausible since ZnO NW core diameters are considerably larger than 10 nm [21] and no blueshift is observed in the UV-PL peak in figure 4. Hence, we conclude that, in contrast to S1 and S2 where $r' \approx 10r$, for S3 we have $r' \lesssim r$, implying that uncorrelated holes and electrons are not much more exposed to non-radiative recombination channels than excitons in this sample and/or have reduced τ_{R}. This is consistent with a very efficient passivation of non-radiative recombination centres at the ZnO NW surface by the MgO shell (increased τ_{NR}) and photocarrier confinement within the ZnO core (which would reduce τ_{R}), leading to enhanced UV emission.

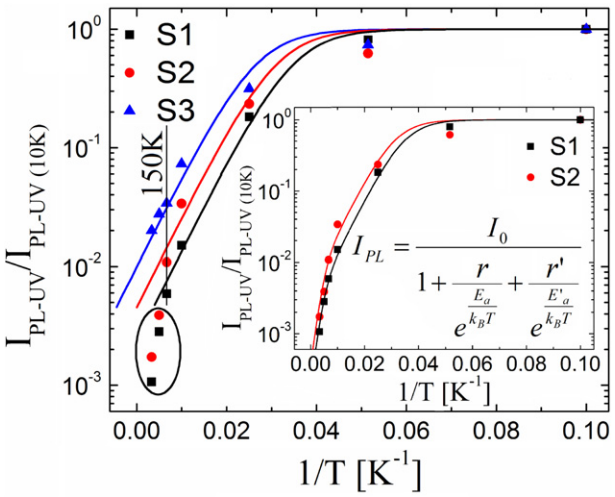

Figure 7. $I_{\mathrm{PL-UV}}$ as a function of the reciprocal temperature for samples S1, S2, and S3. Data sets are normalized by their corresponding values at 10 K. Solid lines at the main graph fit the data using equation (2). The encircled data points from samples S1 and S2 indicate the presence of an additional non-radiative mechanism, significant above 150 K. The inset shows the data from samples S1 and S2 fitted by using equation (3).

5. Conclusion

ZnO/MgO (core/shell) NWs were successfully grown through VTD synthesis. The effects of the MgO shell and (Zn, Mg) interdiffusion across the core/shell interface on the ZnO core emission properties were studied. The thermal quenching of the UV PL is greatly mitigated (as compared to bare ZnO NWs) when the MgO shell is fabricated at $T_{\mathrm{MgO}} \approx 700\,^{\circ}\mathrm{C}$ (S3) and dominated by a single activation energy of 15 meV, corresponding to bound exciton localization energy, in the whole 10–300 K temperature range. The thermal quenching is eliminated almost completely for the visible part of the PL spectrum in the ZnO/MgO core/shell structure, emphasizing the dominating role of the ZnO NW core surface states on both, thermal quenching and emission in the visible. The MgO shell greatly increases UV emission and reduces significantly defect related emission and the radiative to non-radiative recombination lifetime ratio, most likely due to the passivation of visible radiative and non-radiative recombination channels associated with ZnO NW core surface states and photocarrier confinement provided by the MgO shell potential barrier. The above beneficial effects are significantly reduced in NW samples where the ZnO/MgO interface is degraded when allowing some (Mg, Zn) interdiffusion across it at $T_{\mathrm{MgO}} \approx 1000\,^{\circ}\mathrm{C}$. In these samples, additional non-radiative recombination channels become available for temperatures above 150 K as a result of free excitons breakup into

uncorrelated electron–hole pairs. These results should be important in defining NW growth conditions of high quality surface-passivated ZnO NWs for various optoelectronic and photonic applications.

Acknowledgments

The authors would like to thank BSc T Michalsky and Dr R Schmidt-Grund from the Semiconductor Physics Group, University of Leipzig, Germany, for valuable help with the MgZnO bandgap PL measurements, and Dipl. A Setzer from the Division of Superconductivity and Magnetism, University of Leipzig, Germany, for XRD data acquisition. In Argentina, this work was supported by CIUNT (26/E419 and 26/E439) and FONCyT (BID PICT 2010 No. 400).

References

[1] Djurišić A B, Hang Leung X C Y and Ching Ng A M 2012 *J. Mater. Chem.* **22** 6526
[2] Yang Y, Sun X W, Tay B K, Cao P H T, Wang J X and Zhang X H 2008 *J. Appl. Phys.* **103** 064307
[3] Grinblat G, Capeluto M G, Tirado M, Bragas A V and Comedi D 2012 *Appl. Phys. Lett.* **100** 233116
[4] Yang H Y, Yu S F, Li G P and Wu T 2010 *Opt. Express* **18** 13647
[5] Wu Y, Wu W, Zou X M, Xu L and Li J C 2012 *Mater. Lett.* **84** 147
[6] Liu C Y, Xu H Y, Ma J G, Li X H, Zhang X T, Liu Y C and Mu R 2011 *Appl. Phys. Lett.* **99** 063115
[7] Vega N C, Wallar R, Caram J, Grinblat G, Tirado M, LaPierre R R and Comedi D 2012 *Nanothechnology* **23** 275602
[8] Zhang X, Xue D, Wang J and Feng X 2006 *J. Cryst. Growth* **292** 505
[9] Park W I, Yi G-C and Jang H M 2001 *Appl. Phys. Lett.* **79** 2022
[10] Ahirwar V P, Misra P and Ahirwar G 2013 *Res. J. Phys. Sci.* **1** 11
[11] Das A K 2013 arXiv:1302.4246[cond-mtrl-sci]
[12] Ohtomo A, Shiroki R, Ohkubo I, Koinuma H and Kawasaki M 1999 *Appl. Phys. Lett.* **75** 4088
[13] Limpijumnong S, Jutimoosik J, Palakawong N, Klysubun W, Nukeaw J, Du M-H and Rujirawat S 2011 *Appl. Phys. Lett.* **99** 261901
[14] Chen R, Ye Q-L, He T C, Wu T and Sun H D 2011 *Appl. Phys. Lett.* **98** 241916
[15] Wei B, Zheng K, Ji Y, Zhang Y, Zhang Z and Han X 2012 *Nano Lett.* **12** 4595
[16] Park W I, Yoo J, Kim D-W, Yi G-C and Kim M 2006 *J. Phys. Chem.* B **110** 1516
[17] Yoo J, Chon B, Tang W, Joo T, Dang L S and Yi G-C 2012 *Appl. Phys. Lett.* **100** 223103
[18] Hamby D W, Lucca D A, Klopfstein M J and Cantwell G 2003 *J. Appl. Phys.* **93** 3214
[19] Leroux M, Grandjean N, Beaumont B, Nataf G, Semond F, Massies J and Gibart P 1999 *J. Appl. Phys.* **86** 3721
[20] Teke A, Özgür Ü, Doğan S, Gu X and Morkoç H 2004 *Phys. Rev.* B **70** 195207
[21] Sun H D, Makino T, Segawa Y, Kawasaki M, Ohtomo A, Tamura K and Koinuma H 2002 *J. Appl. Phys.* **91** 1993